InterPore JOURNAL

MODELING OF HYDRAULIC FRACTURE PROPAGATION IN REAL HETERO-GENEOUS CONGLOMERATES FROM THE MAHU OILFIELD USING THE GLOBAL COHESIVE ZONE METHOD

Mingyang Zhang [1#], Yanying Chen[2#], Ming Yue[2], Ninghong Jia[3], Weifeng Lyu[3], Amer Alizadeh[4], Haoran Cheng[5,6], Chiyu Xie[*1,7,8]

[1] School of Astronautics, Beihang University, Beijing, China; [2] School of Civil and Resource Engineering, University of Science and Technology Beijing, Beijing, China; [3]Research Institute of Petroleum Exploration and Development, PetroChina, Beijing, China; [4]College of Engineering and Physical Sciences, University of Birmingham, Birmingham, UK; [5]Sichuan Energy Internet Research Institute Tsinghua University, Chengdu, Sichuan, China; [6]School of Chemical Engineering, Qingdao University of Science and Technology, Qingdao, Shandong, China; [7]State Key Laboratory of High-Efficiency Reusable Aerospace Transportation Technology, Beijing, China; [8]Ningbo Institute of Technology, Beihang University, Ningbo, China

[#]These authors contributed equally to the work

APPENDIX I: MATERIAL PROPERTY

Table S1: Parameters used in the physical experiment and numerical simulation.

Parameters	Reference (41)	Present simulation
Young's modulus of matrix $\boldsymbol{E_m}$ (GPa)	36.7	36.7
Poisson's ratio of matrix $\boldsymbol{\nu_m}$	0.248	0.248
Tensile strength of matrix $\boldsymbol{\sigma_m}$ (MPa)	8.1	8.1
Shear strength of matrix $\boldsymbol{\tau_m}$ (MPa)	-	20
Tensile fracture energy of matrix $\boldsymbol{G_m^{IC}}$ ($\mathrm{J/m^2}$)	-	1
Shear fracture energy of matrix $\boldsymbol{G_m^{IIC}}$ ($\mathrm{J/m^2}$)	-	80
Tensile strength of interface $\boldsymbol{\sigma_i}$ (MPa)	7.4	7.4
Shear strength of interface $\boldsymbol{\tau_i}$ (MPa)	-	15
Tensile fracture energy of interface $\boldsymbol{G_i^{C}}$ ($\mathrm{J/m^2}$)	-	0.1
Shear fracture energy of interface $\boldsymbol{G_i^{IIC}}$ ($\mathrm{J/m^2}$)	-	20
Maximum horizontal stress (MPa)	15	15
Minimum horizontal stress (MPa)	5	5
Young's modulus of gravel $\boldsymbol{E_r}$ (GPa)	50.1	50.1
Poisson's ratio of gravel $\boldsymbol{\nu_r}$	0.247	0.247
Tensile strength of gravel $\boldsymbol{\sigma_n^0}$ (MPa)	12.4	12.4
Shear strength of gravel $\boldsymbol{\sigma_s^0}$ (MPa)	-	30
Tensile fracture energy of gravel $\boldsymbol{G_r^{C}}$ ($\mathrm{J/m^2}$)	-	5
Shear fracture energy of gravel $\boldsymbol{G_r^{IIC}}$ ($\mathrm{J/m^2}$)	-	100
Fluid viscosity $\boldsymbol{\mu}$ (mPa-s)	120	120
Injection rate $\boldsymbol{q}$ (ml/min)	20	20
The dimensions of the model (m)	-	0.4 × 0.3
Porosity of matrix	-	0.1
Leak-off coefficient (m^3 /s/Pa)	-	1E-14

https://doi.org/10.69631/taka2w77

Table S2: Simulation Parameters for the Homogeneous Core Model.							
Mineral Name	**Material**	**Young's Modulus /GPa**	**Poisson's Ratio**	**Tensile strength /Mpa**	**Shear strength /MPa**	**Tensile fracture energy/ (J/㎡)**	**Shear fracture energy/ (J/㎡)**
Quartz	Gravel	95	0.07	12	120	4	1000
Albite	Gravel	69	0.28	8	80	2.67	667.5
	Interface	-	-	4	40	0.08	80
K-feldspar	Gravel	91.78	0.28	2	20	0.67	167.5
	Interface	-	-	1	10	0.02	20
Chlorite	Gravel	38.9	0.2	12	120	4	1000
	Interface	-	-	6	60	0.12	120

Table S3: Simulation Parameters for the Heterogeneous Core Model.							
Mineral Name	**Material**	**Young's Modulus /GPa**	**Poisson's Ratio**	**Tensile strength /Mpa**	**Shear strength /MPa**	**Tensile fracture energy/ (J/㎡)**	**Shear fracture energy/ (J/㎡)**
Quartz	Gravel	95	0.07	12	120	4	1000
Illite	Gravel	43.88	0.236	2.16	21.6	0.72	180
	Interface	-	-	1.08	10.8	0.0216	21.6
Kaolinite	Gravel	120	0.24	10.6	106	3.53	882.5
	Interface	-	-	5.3	53	0.106	106
Albite	Gravel	69	0.28	8	80	2.67	667.5
	Interface	-	-	4	40	0.08	80
Quartz-albite-illite mixed gravel	Gravel	69.29	0.195	7.39	73.9	2.46	615
	Interface	-	-	3.695	36.95	0.0739	73.9
Illite-kaolinite mixed gravel	Gravel	81.94	0.238	6.38	63.8	2.13	532.5
	Interface	-	-	3.19	31.9	0.0638	63.8

Appendix II: The workflow for 3D model creation from CT images

Cylindrical microsamples with a diameter of 25 mm were drilled from the selected area on the cylinder core plug and placed into an X-ray CT scanner for microsample scanning with a scanning resolution of micron.

After reconstruction of the scanned data, a 3D grayscale image of the core sample was obtained, as shown below:

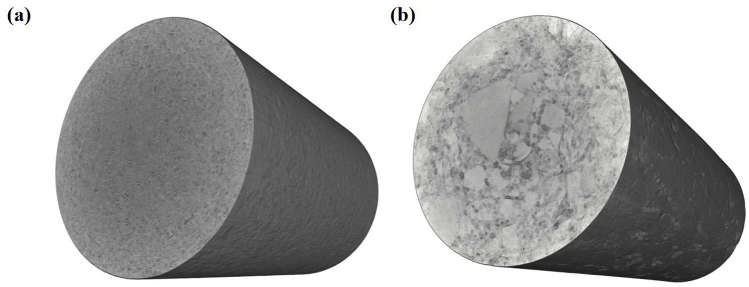

Figure S1: Three-dimensional grayscale images of the (a) homogeneous and (b) heterogeneous cores.

Avizo software was used to perform 3D digital core reconstruction of the CT scan images of both homogeneous and heterogeneous cores. The software's image segmentation tools were then applied to binarize the reconstructed grayscale images, separating the pore space from the solid matrix and obtaining the binary pore distribution (as shown in **Fig. S2**).

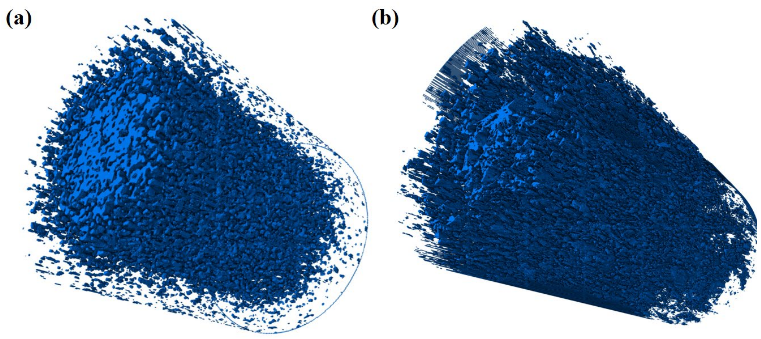

Figure S2: Three-dimensional pore models of the (a) homogeneous and (b) heterogeneous cores.